JTTEES 7:374-382

Computational Fluid Dynamics Analysis of a Wire-Feed, High-Velocity Oxygen Fuel (HVOF) Thermal Spray Torch*

A.R. Lopez, B. Hassan, W.L. Oberkampf, R.A. Neiser, and T.J. Roemer

(Submitted 28 November 1996; in revised form 1 May 1998)

The fluid and particle dynamics of a high-velocity oxygen fuel (HVOF) thermal spray torch are analyzed using computational and experimental techniques. Three-dimensional computational fluid dynamics (CFD) results are presented for a curved aircap used for coating interior surfaces such as engine cylinder bores. The device analyzed is similar to the Metco diamond jet rotating wire (DJRW) torch. The feed gases are injected through an axisymmetric nozzle into the curved aircap. Premixed propylene and oxygen are introduced from an annulus in the nozzle, while cooling air is injected between the nozzle and the interior wall of the aircap. The combustion process is modeled using a single-step, finite-rate chemistry model with a total of nine gas species which includes dissociation of combustion products. A continually fed steel wire passes through the center of the nozzle, and melting occurs at a conical tip near the exit of the aircap. Wire melting is simulated computationally by injecting liquid steel particles into the flow field near the tip of the wire. Experimental particle velocity measurements during wire feed were also taken using a laser two-focus (L2F) velocimeter system. Flow fields inside and outside the aircap are presented, and particle velocity predictions are compared with experimental measurements outside of the aircap.

Keywords CFD, experimental data, HVOF, thermal spray, two-phase flow

1. Introduction

High-velocity oxygen fuel (HVOF) thermal spraying uses a combustion process to heat the gas flow and coating material. The two phase gas and particle flow is then accelerated to high velocities outside of the torch. HVOF torches normally produce temperatures around 3000 K; whereas, in plasma spraying, they are typically around 10,000 K. A lower temperature range causes the gas density in HVOF torches to be higher than in plasma torches. The combination of high gas density and high gas velocity tends to produce higher density coatings.

Because of recent advances in computational fluid dynamics (CFD) methods and computer power, CFD codes can now be used to simulate the HVOF spraying process. The first CFD simulations of the HVOF process were conducted by Power et al. (Ref 1, 2) and Smith et al. (Ref 3). They performed an axisymmetric analysis of the internal flow and external flow of the Metco DJRW torch (Sulzer Metco, Westbury, NY) with a powder feeder. For the internal flow, a two-step, finite-rate chemistry model was used to model the combustion of propylene (C_3H_6). For the external flow, the flow at the exit was assumed to have reached chemical equilibrium so no chemical kinetics were modeled. Inside the aircap, tracker particles of various sizes were injected. These particles were affected by the local gas velocity and temperature, but the gas stream was not affected.

Oberkampf and Talpallikar (Ref 4, 5) also analyzed the fluid and particle dynamics of a similar axisymmetric geometry. The HVOF process was modeled with full coupling between the interior and exterior flow fields. A one-equation, approximate equilibrium chemistry model was used to model the combustion of propylene. An Eulerian-Lagrangian approach was used to model the gas and solid phases, respectively. The gas and particles were fully coupled through momentum and energy exchanges.

Hassan et al. (Ref 6) analyzed the gas flow field of an axisymmetric thermal spray device. The HVOF process was also modeled with full coupling between the interior and exterior flow fields. Both a 1 step and a 12 step quasi-global finite-rate chemistry model were used to model the combustion of propylene. The CFD results compared well with experimental measurements of pressure inside the HVOF aircap for supersonic flow, but the pressure for subsonic flow was somewhat underpredicted. It was found that the 1 step chemistry model compared very well with the 12 step chemistry model, and it was shown to be applicable for predicting thermal spray combustion chemistry (Ref 6).

Hassan, Lopez, and Oberkampf (Ref 7) performed the first three-dimensional analysis of a thermal spray device. The gas flow in the aircap and external to the aircap were simulated with full coupling between the interior and exterior flow fields. An approximate equilibrium chemistry model was used to model the combustion process. Gas flow fields both inside and outside the aircap were presented and discussed.

A.R. Lopez, B. Hassan, W.L. Oberkampf, and **R.A. Neiser,** Sandia National Laboratories, Albuquerque, New Mexico, USA; and **T.J. Roemer,** Ktech Corporation, Albuquerque, New Mexico, USA. Contact e-mail: arlopez@sandia.gov.

*This work was performed at Sandia National Laboratories, which is operated by Lockheed Martin for the U.S. Department of Energy under contract DE-AC04-94AL85000.

The present work shows the first CFD calculations made on a three-dimensional aircap with wire feed. The aircap geometry is similar to the Metco DJRW torch. A solid model representation of this aircap is shown in Fig. 1. This work describes the general gas dynamic features of the complex, three-dimensional flow field as well as the particle dynamic features of the metal particles. An Eulerian-Lagrangian technique is used to couple the fluid dynamics of the gas flow to that of the particles. The gas temperature, Mach number distributions, and streamline patterns are predicted inside and outside the torch. Experimental particle velocity measurements were also taken using an L2F velocimeter system. Particle velocity measurements were obtained in the plane of symmetry of the aircap and compared with the CFD predictions.

2. Gas Dynamics Modeling

The numerical simulations are made using a commercial CFD code, CFD-ACE (Ref 8, 9). CFD-ACE is a pressure-based code that solves the three-dimensional, Favre-averaged Navier-Stokes equations. These equations model the conservation of mass, momentum, and energy for unsteady, compressible, turbulent flows. The governing equations are solved sequentially in an implicit, iterative manner using a finite volume formulation. Various options for modeling turbulence, reaction chemistry, and multiphase flows are available in this code. In the present calculations, the governing equations are solved until a steady-state solution is reached. The governing equations include species transport equations, as there are multiple flow mixtures that are modeled in the present calculation. The k-ε turbulence model of Launder and Spalding (Ref 10) is used along with the compressibility correction of Sarkar (Ref 11). For further details on the numerical algorithms, see Ref 8 and 9.

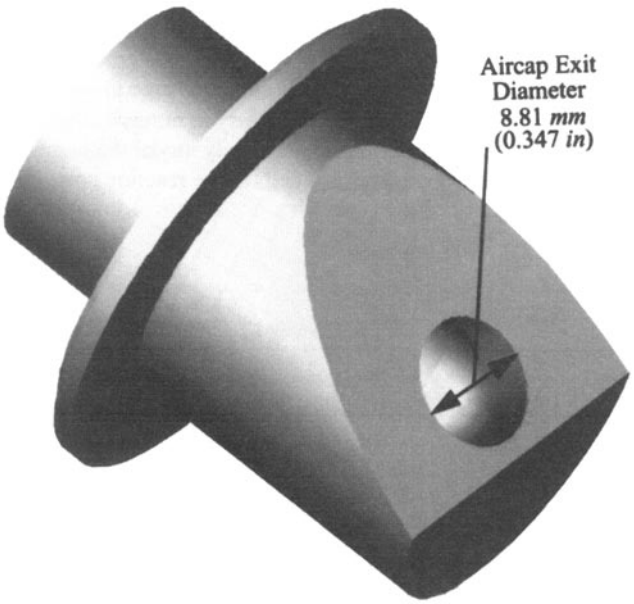

Fig. 1 Solid model of 3-D aircap

3. Chemistry Modeling

The number of intermediate gas species and reactions used in hydrocarbon-oxygen reaction models vary greatly, depending on the model requirements. Given that computer time is greatly increased with the solution of multiple-step chemistry models, the present approach uses a single-step finite-rate chemistry model to represent the hydrocarbon combustion process inside the aircap. Hassan et al. (Ref 6) found that equilibrium chemistry and its approximations produced numerical solutions whose energy release was dependent on spatial grid size. They determined that as the grid spacing in the chemical reaction cell was reduced, the heat release was confined to a smaller region, which resulted in a very high, unrealistic, inlet pressure. Therefore, it was necessary to use a chemistry model that spreads out the heat release over distance, just as it occurs physically. While a 12 step chemistry model includes more intermediate reactions, Hassan et al. (Ref 6) determined that a 1 step chemistry model adequately represented the combustion of propylene. In the present analysis, a fully mixed fuel and oxygen stream was also assumed in order to begin the simulation inside the aircap. The validity of this assumption, however, is difficult to determine.

The 1 step reaction was derived from the one-dimensional equilibrium chemistry code developed by Gordon and McBride (Ref 12) and is of the form:

$$C_3H_6 + xO_2 \rightarrow \text{Products}$$

where x is the number of moles of oxygen that react with one mole of propylene. The products of combustion included CO_2, H_2O, CO, H_2, OH, H, and O. Nitrogen (N_2) was assumed inert at the temperatures considered. Given a specified fuel-oxygen mixture ratio, pressure, and temperature (those of the premixed fuel and oxygen stream), the one-dimensional equilibrium chemistry code (Ref 12) determined the equilibrium composition that is shown by the following balanced reaction:

$$C_3H_6 + 3.6646\,O_2 \rightarrow 1.0924\,CO_2 + 1.9076\,CO + 1.9432\,H_2O + 0.8215\,OH + 0.4329\,H_2 + 0.4263\,H + 0.4721\,O$$

The reaction rate, k_f, used in this investigation is from the work of Westbrook and Dryer (Ref 13) and is defined as follows:

$$k_f = AT^{\eta} \exp(E_a/(RT))[C_3H_6]^a[O_2]^b$$

where T is the local gas temperature, E_a is the activation energy, and A, η, R, a, and b are constants. The reaction constants given by Westbrook and Dryer (Ref 13) were originally calibrated for laminar diffusion flames at different flow conditions. Therefore, some adjustments in these constants were necessary to model turbulent flames. For example, the pre-exponential factor, A, was adjusted in order to match the experimentally observed flame length inside the thermal spray torch. The value of A and all of the reaction constants used were the same as given by Hassan et al. (Ref 6).

4. Liquid Particle Modeling

The liquid droplet equations are solved in a Lagrangian frame of reference moving with the particles. The solutions to

these equations are used to calculate the source/sink terms for the corresponding gas phase equations, which are solved in an Eulerian frame of reference. The dominant coupling between the particle and gas phases is due to momentum transfer; energy coupling is secondary. The equation of motion for the particle is written as (Ref 14):

$$m_p \frac{d\mathbf{U}_p}{dt} = \frac{1}{2} \rho A_p C_d (\mathbf{U} - \mathbf{U}_p)|\mathbf{U} - \mathbf{U}_p| - \mathbf{V}_p \Delta p$$

where m_p is the mass of the particle and $\mathbf{U}_p$ is the velocity vector of the particle. C_d is the drag coefficient, and ρ, $\mathbf{U}$, and p are the density, velocity, and pressure of the gas, respectively. A_p is the particle surface area and V_p is the particle volume. The liquid particles are assumed to be spherical during their entire trajectory. The equation of motion for a particle accounts for the acceleration/deceleration of the particle due to the combined effects of drag from the gas flow and local pressure gradients of the gas. In addition, an energy equation coupling the particles and the gas is solved but is not presented.

The drag coefficient for the particle is a function of the local Reynolds number of the particle which is evaluated as:

$$Re = \frac{\rho |U - \mathbf{U}_p| d_p}{\mu}$$

where d_p is particle diameter and μ is the molecular viscosity of the local gas mixture. The following correlations have been found to be valid for a wide range of Reynolds numbers (Ref 14):

$$C_d = \frac{24}{Re} \qquad \text{for } Re < 1$$

$$C_d = \frac{24}{Re}(1 + 0.15\, Re^{0.67}) \qquad \text{for } 1 < Re < 10^3$$

$$C_d = 0.44 \qquad \text{for } Re > 10^3$$

These drag coefficient relations have been shown to be reliable for particle Mach numbers less than unity, relative to the local gas speed of sound. The relative Mach number of the particle is given by:

$$M_p = \frac{|\mathbf{U} - \mathbf{U}_p|}{\sqrt{\gamma R T}}$$

where γ is the ratio of specific heats of the gas, R is the gas constant, and T is the gas temperature. γ, R, and T are all evaluated at the particle location and are dependent on the local mixture of gas species.

5. Aircap and Grid Generation

The geometry of the aircap is similar to a Metco DJRW torch. Figure 2 shows a computational grid in the plane of symmetry of the curved aircap. The interior of the aircap is composed of a converging conical section and two cylindrical sections that are blended together by a portion of a sphere. The turn angle between the two cylinder centerlines is 60°. There are two sets of inlet streams: the premixed fuel and oxygen stream, and the annular air cooling stream along the surface of the aircap. In the Metco hardware, the fuel-oxygen stream is fed into the aircap by ten equally spaced holes around the nozzle just inside the circumferential lip of the nozzle. In the present analysis, the fuel-oxygen inlet is modeled as an annulus that has the same total area as the ten holes and is centered at the same radial location as the holes in the nozzle. This assumption greatly simplifies the numerical simulation by reducing the size of the aircap grid in the circumferential direction. It should be noted that while the geometry of the nozzle holes is no longer fully three-dimensional (3-D), the remaining aircap geometry is 3-D and the flow field that develops is 3-D.

Figure 2 also shows a steel wire positioned in the aircap. The centerlines of the nozzle and the metal wire have been shifted vertically upward by 0.406 mm (0.016 in.) from the centerline of the conical portion of the aircap. This shift is necessary to provide more air cooling flow to the bottom portion of the aircap where the highest heat transfer rates would occur without an offset. Both the premixed fuel-oxygen and the air cooling streams are angled 5° to the centerline of the nozzle.

At the inlet face of the torch in Fig. 2, the inner radius of the aircap is 5.59 mm (0.22 in.) and the outer radius of the nozzle is 4.13 mm (0.1625 in.). The outer radius of the fuel-oxygen annulus is 3.10 mm (0.1222 in.) and the inner radius is 2.79 mm (0.1098 in.). The radius of the metal wire is 1.59 mm (0.0625 in.), and the aircap exit diameter is 8.81 mm (0.347 in.).

GRIDGEN Version 10 (Ref 15) was used to generate the computational grid used in the CFD calculations. The interior grid shown in Fig. 2 was created in three blocks: the air inlet section, the fuel-oxygen inlet section, and the remaining aircap section up to the exit. Because of symmetry about the centerline plane, only half of the aircap was simulated. Figure 2 shows the radial grid clustering that was used to resolve the shear layers surrounding the fuel-oxygen inlets, the edge of the flame, and the boundary layers along the surface of the aircap and the wire. In the axial direction, the grid points were clustered near the fuel-oxygen inlet and then gradually stretched toward the exit of the aircap. Axial clustering was necessary to numerically stabilize the combustion process and accurately model the large energy release in the computational cells of the reaction zone. The

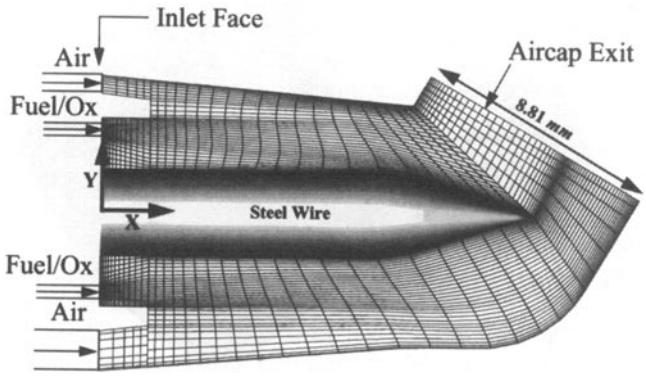

Fig. 2 Interior aircap grid in plane of symmetry (every other grid line shown)

grid was also clustered on the leeside of the conical tip to capture the wake flow off of the wire. The number of grid points in the interior of the aircap are 26 (axial) by 41 (radial) by 20 (circumferential) in the fuel-oxygen inlet section, 12 (axial) by 16 (radial) by 20 (circumferential) in the air inlet section, and 56 (axial) by 65 (radial) by 20 (circumferential) in the remaining aircap section.

Figure 3 shows the exterior grid in the plane of symmetry outside of the aircap. The upper and lower boundaries extend 13 aircap exit radii from the centerline and the outlet boundary extends 14 aircap exit radii from the aircap exit. For simplicity of boundary conditions, a solid circular wall was assumed in the exit plane of the aircap. Grid points were highly clustered in the jet decay region outside the torch as shown by the solid black region in Fig. 3. In addition, the exterior grid lines were tilted downward from the geometric centerline of the aircap exit plane, in order to better align the grid with the expected jet flow direction. The number of grid points in the exterior of the aircap are 71 (axial) by 86 (radial) by 20 (circumferential). The total number of grid points (in the half-volume), interior and exterior to the aircap was 220,080 for this 3-D calculation.

6. Boundary Conditions

Table 1 lists the mass flow rates and gas temperatures that were specified at each inlet in the present simulation. All of the interior walls of the aircap, nozzle, and wire surface are modeled with a no-slip, fixed temperature condition. The wall temperature on all surfaces of the nozzle was specified to be 850 K based on a conduction-convection analysis. The wall temperature of the aircap was specified to be 305 K based on experimental measurements. The turbulent length scales of the inlet streams were based on the physical size of the inlets, and a 10% turbulence intensity. To determine the actual turbulent values would require modeling the flow in the fuel, oxygen, and air feeder tubes. The turbulent values used in the simulation are given in Table 2.

In the actual Metco device, wire is continually fed at a constant rate such that the wire tip remains fixed relative to the aircap. This allows the wire to be modeled as a fixed no-slip wall. A linear temperature distribution is specified along the wire that varies from 330 K at the inlet to 1780 K at the shoulder of the wire (i.e., at the beginning of the wire tip). Since the steel wire is melting along the tip, a constant value of 1780 K was assumed on the conical tip. The value at the inlet was chosen to be slightly higher than ambient temperature due to heat conduction through the nozzle. The value at the conical tip is the melting temperature of steel.

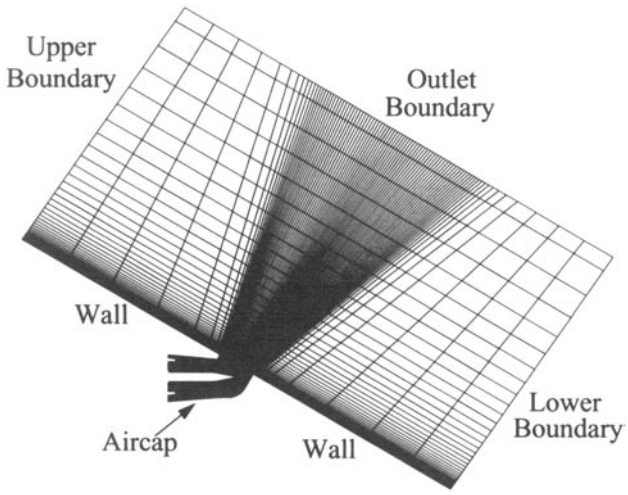

Fig. 3 Exterior grid in plane of symmetry (every other grid line shown)

The HVOF torch is assumed to exhaust into ambient air at a temperature of 303 K and a pressure of 83427 Pa, atmospheric pressure for Albuquerque, New Mexico, where the experimental data were taken. In the exterior grid, the boundary surrounding the aircap exit is specified to be a fixed temperature, no-slip wall. The upper and lower outer boundary is specified to be a fixed pressure inlet/outlet and the outlet boundary is specified to be a zero-pressure gradient outlet. In the plane of symmetry, a symmetry condition is specified for both the interior and exterior domains.

In the Metco device, a liquid layer of steel forms along the conical tip as the wire melts. The droplets are then stripped off the actual tip of the wire by the surface shear stress of the gas acting on the liquid layer. In the present simulation, the stripping of the liquid droplets from the wire tip is modeled as ten steel particles continually injected along the leeside of the conical tip near the plane of symmetry. The small number of computational particles, as compared to the number of physical particles, is not critically important for adequate simulations. The important parameter to match in the simulation is the mass flow rate of the particles. The particle size is 30 μm, the temperature is 1900 K, and the velocity is zero for initial conditions at each injection point. The particle size was based on phase Doppler particle analyzer (PDPA) measurements in previous experiments which produced a number geometric mean diameter of approximately 30 μm. Note that this experimental measurement was outside the aircap, after droplet break-up was complete. The initial particle temperature was chosen to be 120° higher than the melt temperature because it is assumed that some particle superheating occurs in flight; however, the numerical results were not sensitive to particle temperature. The mass loading is based on a 40 in./min wire feed rate which results in a 1.054×10^{-3} kg/s mass flow rate of the particles. Given the mass flow rate and the size of the steel particles, the number of particles per second in the

Table 1 Mass flow rates and inlet temperatures

Gas	Mass flow rates SCFH	Mass flow rates kg/s	Temperature, K
Propylene	100.0	1.350×10^{-3}	450.0
Oxygen	450.0	4.630×10^{-3}	450.0
Air	1100.0	1.024×10^{-2}	330.0

Table 2 Turbulent kinetic energy and dissipation

Inlet	Turbulent kinetic energy, $k = m^2/s^2$	Dissipation rate, $\varepsilon = m^2/s^3$
Fuel/oxygen	2600	9.840×10^8
Air	120	2.920×10^6

problem is close to 1 billion. In order to keep the simulation to a reasonable size, 10 particles were arbitrarily chosen to represent all the particles in the flow such that one computational particle simulates approximately half a million physical particles. The mass flow rate of each computational particle, $\dot{m}_p$, is determined from the total mass flow rate, $\dot{m}_T$, as follows:

$$\dot{m}_p = \left(\frac{1}{2}\dot{m}_T\right)\left(\frac{10}{180}\right)/10$$

Since only half of the aircap is simulated due to geometric symmetry, the total mass flow rate is divided by two to obtain the correct mass flow rate for this simulation. In addition, the effective cross-sectional area through which the particles flow is reduced from a 180° section to a 10° section because the particles are injected along a line that is parallel to the conical tip of the wire. Finally, the mass flow rate is divided by ten in order to determine the mass flow rate of each computational particle.

7. Computational Requirements

The computational simulations were run until all residuals dropped 4 to 5 orders of magnitude over the computational domain. Typically, 3000 iterations are required to obtain 4 to 5 orders of magnitude reduction in the residuals. These simulations involved multiple restarts to improve input parameters and grid quality. The solution required 3.0 ms/cell/iteration of CPU time and 250 MB of RAM on a SPARCstation 10 Model HS125 work station (Sun Microsystems, Palo Alto, CA). These 3000 iterations required a total CPU time of 500 h (~3 weeks). However, the computational times can vary greatly depending on the optimization parameters chosen for solution convergence.

8. Experimental Measurements

The experimental data were taken in the Thermal Spray Research Laboratory at Sandia National Laboratories. Gas flows to the Metco DJRW torch were set using a Metco ATC controller (Sulzer Metco, Wesbury, NY). The ATC uses Hasting-Teledyne 200 Series mass-flow controllers (Teledyne Hasting-Raydist, Hampton, VA) to meter the gas flow rates. The gas flows used in this experiment are given in Table 1. The wire feed rate was approximately 21 mm/s (50 in./min).

Particle velocity distributions were measured in the HVOF jet using a laser two-focus (L2F) velocimeter. A detailed description of this device has been published previously (Ref 16). The 30 μm particle size used in the simulations was based on PDPA measurements made using similar, but not identical, torch geometries and gas flow rates. However, it has been shown that particle size distributions are relatively insensitive to these process variations (Ref 17). In the simulations presented in this paper, discrete particles of a fixed size are released at various locations in the vicinity of the wire tip. In reality, the wire melting and droplet atomization process produces a particle stream that has size and velocity distributions that vary as a function of position in the jet (Ref 17). A 30 μm size was selected because it is the number geometric mean size of particle size distributions measured several centimeters downstream of the wire tip when atomization is complete. That is, it is the most frequently produced particle size in the plume.

Particle velocity distributions were measured using the L2F velocimeter at each point in the plume. The velocity distributions had a slowly falling high velocity tail associated with finely atomized particles (Ref 17). A single particle velocity needed to be extracted from each velocity distribution for comparison with calculated values. PDPA measurements of particle size-velocity correlations revealed that, for at least the first 5 cm downstream of the wire tip, particle size is essentially independent of particle velocity (Ref 17). For this reason, the mode of the particle velocity distribution (i.e., the most frequently recorded velocity) rather than the mean of the distribution was used. Because of the high velocity tail, the velocity mode was typically about 5% slower than the velocity mean at any given point in the plume.

Experimental measurements of particle velocity were made along a two-dimensional (2-D) grid oriented at a 45° angle with respect to the wire axis. The origin of the grid was at the center of the exit hole in the curved aircap. Measurements were made axially along the jet in 1 cm increments out to 10 cm, and radially in 0.2 cm increments over the range ±0.4 cm. The center of the particle jet followed a trajectory tilted at ~6° with respect to the grid's axial direction. Consequently, some measurements of the densest part of the particle plume at axial distances greater than ~4 cm were not made. Overall, the experimental system demonstrated that the data were reproducible for a variety of conditions such that the uncertainty of the particle velocity data is roughly ±5 m/s.

9. Results

9.1 Internal Flow Field

The computed gas temperature contours in the plane of symmetry of the aircap are shown in Fig. 4. The inflow of the premixed fuel-oxygen stream can be seen as the low temperature (dark blue) regions above and below the wire. Combustion occurs primarily on the inner and outer mixing layers of the annular injection of the premixed fuel and oxygen. The flame is approximately 7 mm long, and the peak temperature in the flow field is 3330 K. Along the top and bottom surface of the aircap, an annular jet of air is injected between the nozzle and the aircap. The air layer on the bottom of the aircap is thicker due to the vertical shift between the nozzle and the aircap. This shift is necessary to keep the bottom curved portion of the aircap from melting. Simulating the gas flow through the aircap with wire feed also produces a wake region above the leeside of the wire tip. In the wake region, the temperature of the gas is reduced approximately 500 K from the surrounding combustion gas temperatures.

Figure 5 shows the streamline pattern in the plane of symmetry of the aircap. Near the inlet, a large recirculation flow region can be seen between the wire and the fuel-oxygen jet and a small region can also be seen between the jet and the nozzle. High temperature combustion products become trapped in the vortical flow which continually ignites the incoming fuel-oxygen stream. A small recirculation region is also seen in the base flow region of the nozzle lip, between the fuel-oxygen inlet and the

air inlet. On the upper surface of the aircap, near the exit, the boundary layer separates from the wall as the flow tries to turn the sharp corner. The streamline pattern shows that flow from the ambient exterior region is sucked into the aircap in the separated region. Finally, Fig. 5 shows that along the cylindrical portion of the wire the flow is essentially axial. However, along the conical tip, crossflow over the tip occurs due to the aircap turning the stream. Sufficient crossflow is generated so that a small separated flow region is formed on the leeside of the wire.

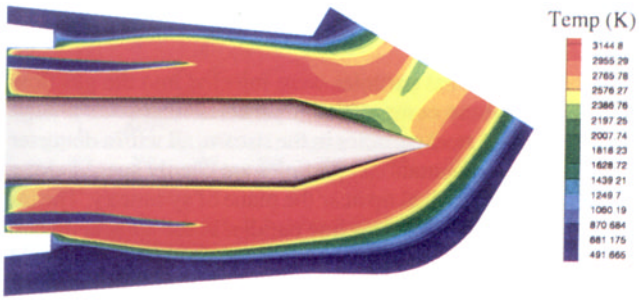

Fig. 4 Plane of symmetry gas temperature contours inside aircap

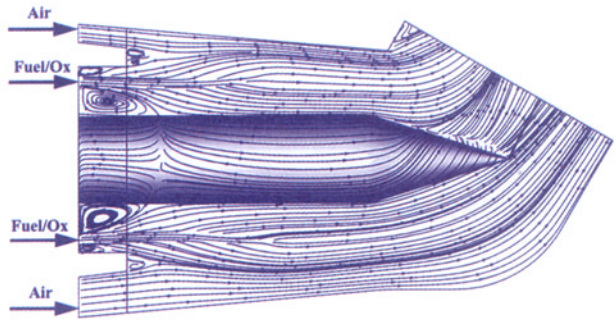

Fig. 5 Plane of symmetry and wire surface streamline pattern inside aircap

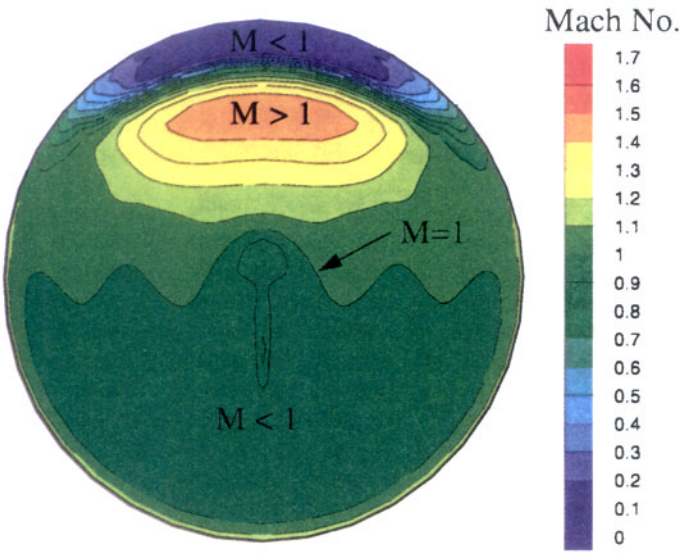

Fig. 6 Gas Mach number contours in the exit plane of the aircap

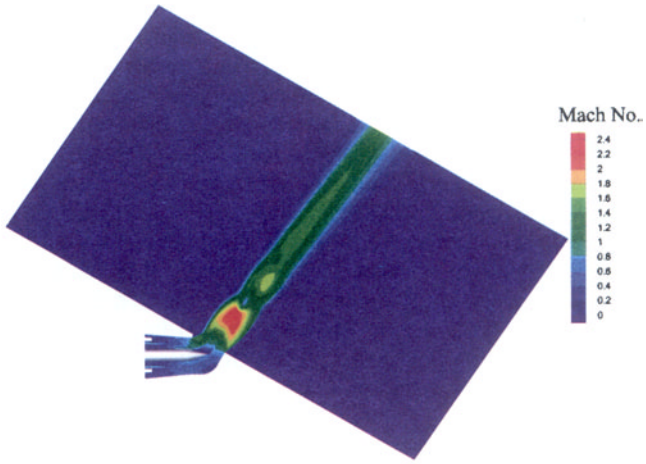

Fig. 7 Gas Mach number contours in the plane of symmetry of the aircap and exterior

Fig. 8 Streamline patterns in the plane of symmetry of the aircap and exterior

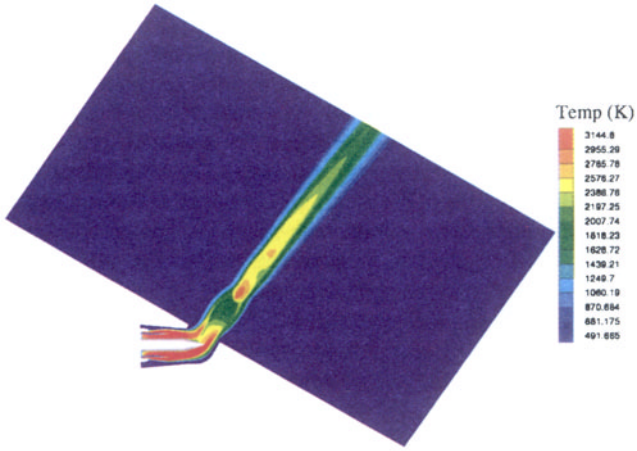

Fig. 9 Gas temperature contours in the plane of symmetry of the aircap and exterior

Figure 6 shows gas Mach number contours in the circular exit plane of the aircap (i.e., normal to the view in Fig 4 and 5). At the top of the aircap exit, there is a subsonic flow region where the ambient air is flowing into the aircap. Between this separated flow region and the middle of the aircap exit, the flow is supersonic. In the lower half of the aircap exit, which is mostly subsonic, there is a spoon-shaped region of lower-speed flow that is caused by the wake flow off of the wire. This figure clearly shows the complex 3-D flow exiting this type of thermal spray torch. There is a range in Mach numbers from low subsonic, where there is reversed flow into the torch, to a peak Mach number of 1.75.

9.2 External Flow Field

Gas Mach number contours in the plane of symmetry are shown in Fig. 7. The peak Mach number in the supersonic jet occurs within one exit diameter from the aircap and has a value of 2.5. The peak Mach number occurs exterior to the torch because the aircap operates as an underexpanded nozzle (i.e., the flow expands to match the ambient pressure outside of the aircap). The Mach number is the ratio of the local gas speed to the local speed of sound. Because of the high gas temperatures in the jet, the local speed of sound is about 1200 m/s at the peak Mach number.

At the exit of the aircap, the flow expands to ambient pressure through a series of expansion and compression waves known as shock diamonds. The first series of waves exterior to the aircap are expansion waves. These waves reflect from the free jet boundaries as compression waves, resulting in the first shock diamond about 1.5 exit diameters from the exit. Only one distinct shock diamond can be seen in the flow field, the dark region of lower Mach number. Increased grid resolution in this region would pick up other diamonds, as was visually observed in the thermal spray flame. The strength of the expansion and compression waves decreases as the flow convects downstream and the supersonic core flow is dissipated as it mixes with the ambient air. The supersonic region, however, extends to the end of the calculation domain.

Streamline patterns overlaid on pressure contours in the plane of symmetry are shown in Fig. 8. The streamline pattern clearly shows the jet flow from the aircap exit to the end of the computational domain. It can be seen that the jet is not aligned normal to the exit plane of the aircap. The jet has been directed downward by the separated shear layer that exists on the upper portion of the aircap near the exit. The predicted spray angle of the torch is approximately 50°; whereas, the geometric turn angle of the aircap is 60°. This is an important difference, for example, in designing a curved aircap for a certain spray angle impinging on an engine cylinder bore. The streamlines also show the entrainment, or pumping, of ambient air from the upper and lower boundaries into the high-speed jet. The peak velocity in the jet is about 2250 m/s and decreases to a value of 1150 m/s at the exit of the computational domain.

Figure 9 shows the gas temperature contours in the plane of symmetry. It can be seen that the gas temperature of the jet decreases as the flow travels downstream due to the turbulent entrainment of the ambient air. At the aircap exit, the peak gas temperature is approximately 3000 K. Then, the temperature drops in the first expansion wave to about 2000 K. Next, the temperature rises in the first shock diamond to about 2250 K. Finally, the temperature decreases to about 1000 K at the exit of the computational domain. These high temperature jets of HVOF torches decay rapidly compared to cold gas jets due to their low density and the rapid entrainment of ambient air. Refer to Ref 18 for additional information.

9.3 Particle Characteristics

Ten computational particles were injected into the gas flow field. Each of these computational particles represents a large number of actual steel particles in the stream, all with a diameter of 30 μm. The computational particles are evenly spaced along the leeside of the conical tip near the plane of symmetry. The injection points, which are on a line parallel to the conical tip, are displaced slightly in a direction normal to the surface to avoid being trapped in the separated flow region shown by the streamline pattern in Fig. 5.

Figure 10 shows the predicted trajectories of the steel particles with respect to a coordinate system aligned with the axis of the nozzle. That is, the x coordinate is aligned with the centerline of the wire and y is normal to the wire, as shown in Fig. 2. The centerline normal to the exit plane of the aircap, shown as a solid line in Fig. 10, starts at the aircap exit (x = 15.870 mm, y = 2.269 mm) and extends to the edge of the computational domain. Particle No. 1 was injected near the tip of the wire, and particle No. 10 was injected near the cylindrical portion of the wire, with the other eight particles in between. As shown in Fig. 10, particles No. 1 to 5 remained closest to the exit centerline, while particles No. 7 to 10 fanned out away from the centerline. Particles No. 1 to 5 were injected near the separated flow region, where the gas had dominant crossflow over the tip, and were immediately swept up by the gas flow toward the exit-plane centerline. Whereas, particles No. 7 to 10 were injected into a higher momentum gas flow primarily aligned with the wire which carried them over the separated flow region and farther away from the exit centerline. Note that all particles were predicted to spray at angles less than the turn angle of the curved aircap. The trajectory for particle No. 6 was almost identical to the trajectory of particle No. 5 and was not included in Fig. 10.

Figure 11 shows the variations of the particle velocities with axial position. The position of the aircap exit is shown as a solid line in this figure. Ahead of the aircap exit, all particle velocities are inside the aircap. The particle velocities increase rapidly as the gas expands outside of the aircap. After a short distance, some of the velocities start to level off (e.g., particle No. 10). The reason for this is that their trajectory has taken them outside the high-velocity spray jet into ambient air. At the end of the computational domain, particle No. 2 has the largest velocity with a value of 310 m/s.

Figure 12 shows a contour plot of the velocity for all ten particles outside of the aircap. The boundaries of the contour plot are based on the position of the particle trajectories from the injection point to the edge of the computational domain. The maximum velocity region is located in the upper portion of the contour plot, near the edge of the computational region. The line of peak particle velocities, at a given axial distance from the aircap exit, is seen at an angle of 10° from the geometric centerline of the aircap exit plane. The reason for this offset is that the peak jet velocities are offset from the geometric centerline. The particle velocities outside of the aircap range between 100 to 310 m/s.

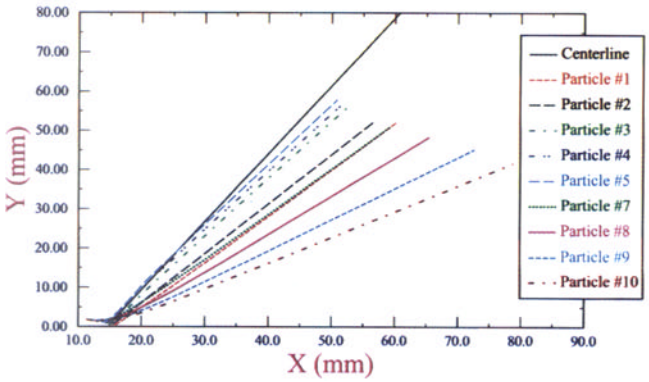

Fig. 10 Predicted particle trajectories relative to the geometric centerline of the aircap exit

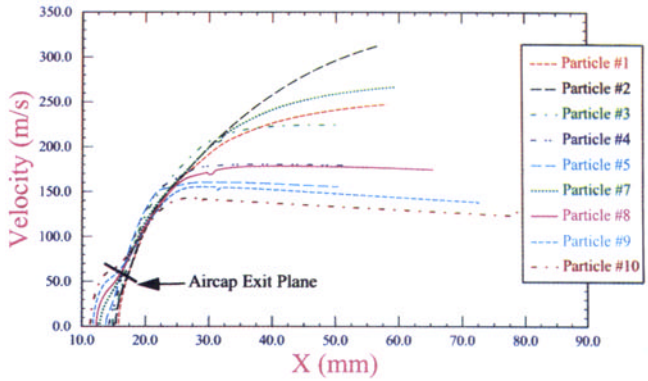

Fig. 11 Predicted particle velocities from wire tip to edge of computational domain

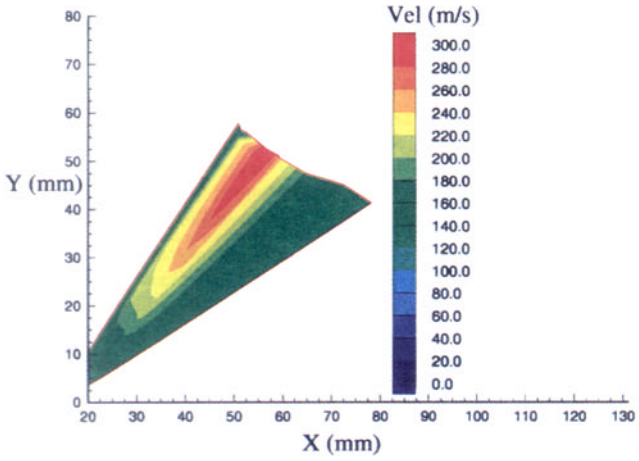

Fig. 12 Particle velocity contours of numerical predictions

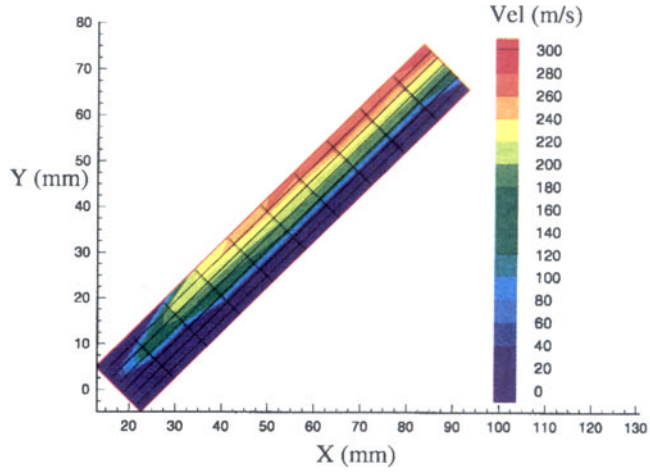

Fig. 13 Paticle velocity contours of experimental data

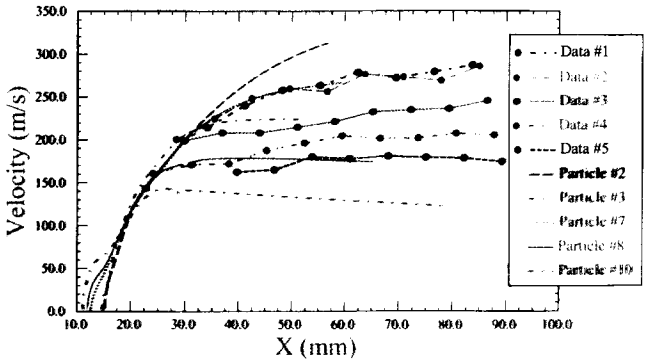

Fig. 14 Particle velocities of both numerical predictions and experimental data

Figure 13 shows a contour plot of the experimentally measured velocities. The 2-D grid overlaid on the velocity contours shows the locations at which the particle velocities were measured. The rectangular measurement region was intended to cover the region of maximum particle velocities, but it did not quite capture the peak velocities. This is why the peak velocities are missing from the upper edge of the plot. This figure also shows zero velocity regions near the aircap exit and along the lower edge of the experimental domain. Zero velocity measurements were the result of having too few particles in these regions to sample, not that the particle velocity is zero.

Figure 14 shows particle velocity curves of both the numerical predictions and the experimental measurements. The experimental data curves are the velocity values along grid lines in the direction of flow. Only nonzero experimental data curves, starting from the upper streamwise edge of Fig. 13, are shown in this figure. A sampling of the predicted velocity curves, including the maximum and minimum curves, are shown. It can be seen from this figure that the numerical results bound the experimental data and display the same trends with x. Note that the numerical results are for individual particles that are tracked throughout the entire domain; whereas, in the experiment, velocities of many different particles are measured at each experimental grid point, and the most frequently recorded value of velocity is computed. In other words, the band of velocities predicted in Fig. 14 is due to various paths, or trajectories, that the particles take. The path that a computational particle follows depends on the initial injection position. In the simulation, the particle injection positions were chosen to ensure that the particle trajectories spanned the region where velocity measurements were taken. Therefore, some of the computational particles did not necessarily simulate the initial position of the real metal droplets.

Table 3 Measured and predicted particle velocities

x, mm	y, mm	Measured V, m/s	Predicted V, m/s	Percent error
22.5	9.3	143.1	147.3	2.9
30.0	16.4	198.9	192.6	3.2
37.1	23.5	208.0	218.1	4.9

Table 3 shows a direct comparison of the numerically predicted and experimentally measured particle velocities at three coincident locations. The three locations chosen are along the data No. 3 grid line which is in the middle of the experimental data. The predictions compare very well with the measured particle velocities up to about 40 mm from the inlet face. Overall, the percent error between the predictions and the measurements is less than 5%.

10. Summary and Conclusions

Numerical and experimental results were presented for an HVOF spray device similar to a Metco DJRW torch. Computational results were presented for the internal combusting flow, the external jet decay, and the wire droplet flow field. Gas temperature, Mach number distributions, streamline patterns, and particle trajectories and velocities were discussed to illustrate features of the complex 3-D flow. The peak temperature in the combustor was 3330 K, and the peak Mach number in the jet was 2.5. L2F measurements were made to determine the wire sprayed particle velocities in the external plume. Very good agreement was obtained between the computational particles and the particle velocity measurements. Note that a 2-D axisymmetric simulation, while computationally faster, would not predict the offset of the particles and the flow field nor would it capture the 3-D features of the flow at the aircap exit and in the jet decay region outside of the aircap.

Future work should include additional validation of the numerical simulations. Experimental measurements of gas velocity, possibly using the L2F technique and submicron particle injection, and gas temperature should be made. Additional validation of several CFD predicted parameters will build confidence in these types of simulations. Although 3-D CFD simulations are complex and very computer intensive, they provide an unparalleled level of physical information concerning these devices. With this level of analysis, these numerical tools can be used to significantly improve and optimize HVOF spray torch designs.

Acknowledgments

The authors wish to thank Fritz Owens and Milind Talpallikar of CFD Research Corporation and Ron Dykhuizen of Sandia National Laboratories for their continued assistance and consultation on the two-phase flow. Also, the authors wish to thank Mark Smith of the Sandia National Laboratories for his assistance with the experimental measurements.

This work was supported under United States Department of Energy, Cooperative Research and Development Agreement No. SC92-01104. This research was conducted jointly with the Powertrain Group of General Motors Corporation.

References

1. G.D. Power, T.J. Barber, and L.M. Chiappetta, "Analysis of High Velocity Oxygen Fuel (HVOF) Thermal Torch," American Institute of Aeronautics and Astronautics, Paper No. 92-3598, July 1992
2. G.D. Power, E.B. Smith, T.J. Barber, and L.M. Chiappetta, "Analysis of a Combustion (HVOF) Spray Deposition Gun," UTRC Report 91-8, East Hartford, CT, March 1991
3. E.B. Smith, G.D. Power, T.J. Barber, and L.M. Chiappetta, Application of Computational Fluid Dynamics to the HVOF Thermal Spray Gun, *Thermal Spray: International Advances in Coatings Technology*, C.C. Berndt, Ed., ASM International, 1992, p 805-810
4. W.L. Oberkampf and M. Talpallikar, Analysis of a High-Velocity Oxygen-Fuel (HVOF) Thermal Spray Torch—Part 1: Numerical Formulation, *J. Therm. Spray Technol.*, Vol 5 (No. 1), 1996, p 53-61
5. W.L. Oberkampf and M. Talpallikar, Analysis of a High-Velocity Oxygen-Fuel (HVOF) Thermal Spray Torch—Part 2: Computational Results, *J. Therm. Spray Technol.*, Vol 5 (No. 1), 1996, p 62-68
6. B. Hassan, W.L. Oberkampf, R.A. Neiser, and T.J. Roemer, "Computational Fluid Dynamic Analysis of a High-Velocity Oxygen-Fuel (HVOF) Thermal Spray Torch," presented at the 8th National Thermal Spray Conference, Sept 1995, Houston, TX
7. B. Hassan, A.R. Lopez, and W.L. Oberkampf, Computational Analysis of a Three Dimensional High-Velocity Oxygen-Fuel (HVOF) Thermal Spray Torch, *Advances in Thermal Spray Science and Technology*, C.C. Berndt and S. Sampath, Ed., ASM International, 1995, p 193-198
8. Y.G. Lai, A.J. Przekwas, and R.M.C. So, "Aerodynamic Flow Simulation Using a Pressure-Based Method and a Two-Equation Turbulence Model," American Institute of Aeronautics and Astronautics, Paper No. 93-2902, July 1993
9. Y. Jiang, Y.G. Lai, S.Y. Ho, and A.J. Przekwas, "3D Simulations of Complex Flows with an Implicit Multi-Domain Approach," American Institute of Aeronautics and Astronautics, Paper No. 93-3124, July 1993
10. B.E. Launder and D.B. Spalding, The Numerical Calculation of Turbulent Flows, *Comput. Methods Applied to Mechanics and Eng.*, Vol 3, 1974, p 269-289
11. S. Sarkar, The Analysis and Modeling of Dilatational Terms in Compressible Turbulence, *J. Fluid Mechanics*, Vol 227, 1991, p 473-493
12. S. Gordon and B.J. McBride, "Computer Program for Calculation of Complex Chemical Equilibrium Compositions, Rocket Performance, Incident and Reflected Shocks, and Chapman-Jouguet Detonations," NASA SP-273, Interim Revision, March 1976 (New Version 1989)
13. C.K. Westbrook and F.L. Dryer, Simplified Reaction Mechanisms for the Oxidation of Hydrocarbon Fuels in Flames, *Combustion of Science and Technology*, Vol 27, 1981, p 31-43
14. C.T. Crowe, M.P. Sharma, and D.E. Stock, "The Particle-Source-In CELL (PSI-CELL) Model for Gas-Droplet Flows," *J. Fluids Eng.* 1977, p 325-332
15. *GRIDGEN User's Manual*, Version 10, Pointwise, Inc., Bedford, TX, March 1995
16. M.F. Smith, T.J. O'Hern, J.E. Brockmann, and R.A. Neiser, A Comparison of Two Laser-Based Diagnostics for Analysis of Particles in Thermal Spray Streams, *Advances in Thermal Spray Science and Technology*, C.C. Berndt and S. Sampath, Ed., ASM International, 1995, p 105-110
17. R.A. Neiser, J.E. Brockmann, T.J. O'Hern, R.C. Dykhuizen, and M.F. Smith, Wire Melting and Droplet Atomization in a HVOF Jet, *Advances in Thermal Spray Science and Technology*, C.C. Berndt and S. Sampath, Ed., ASM International, 1995, p 99-104
18. G.L. Brown and A. Roshko, On Density Effects and Large Scale Structure in Turbulent Mixing Layers, *J. Fluid Mechanics*, Vol 64 (Part 4), 1974, p 775-816